Atmospheric
Chemistry
and Physics
Discussions

Open Access

Investigation of processes controlling GEM oxidation at mid-latitudinal marine, coastal, and inland sites

Z. Ye[1], H. Mao[1], C.-J. Lin[2,3], and S. Y. Kim[4]

[1]Department of Chemistry, State University of New York College of Environmental Science and Forestry, Syracuse, NY 13210, USA
[2]Center for Advances in Water and Air Quality, Lamar University, Beaumont, TX 77710, USA
[3]Department of Civil and Environmental Engineering, Lamar University, Beaumont, TX 77710, USA
[4]R&D Program Evaluation Division Office of National Evaluation and Analysis Korea Institute of S&T Evaluation and Planning (KISTEP), Seoul, South Korea

Correspondence to: Z. Ye (zye01@syr.edu)

ACPD

doi:10.5194/acp-2015-829

Investigation of processes controlling GEM oxidation at mid-latitudinal sites

Z. Ye et al.

Title Page

Abstract | Introduction

Conclusions | References

Tables | Figures

|◄ | ►|

◄ | ►

Back | Close

Full Screen / Esc

Printer-friendly Version

Interactive Discussion

Abstract

A box model incorporating a state-of-the-art chemical mechanism for atmospheric mercury (Hg) cycling was developed to investigate oxidation of gaseous elemental mercury (GEM) at three locations in the northeastern United States: Appledore Island (marine), Thompson Farm (coastal, rural), and Pack Monadnock (inland, rural, elevated). The chemical mechanism improved model's ability to simulate the formation of gaseous oxidized mercury (GOM) at the study sites. At the coastal and inland sites, GEM oxidation was predominated by O_3 and OH, contributing 80–99 % of total GOM production during daytime. H_2O_2 initiated GEM oxidation was significant (~ 33 % of the total GOM) at the inland site during nighttime. In the marine boundary layer (MBL), Br and BrO were dominant GEM oxidants contributing ~ 70 % of the total GOM production during mid-day, while O_3 dominated GEM oxidation (50–90 % of GOM production) over the remaining day. Following the production of HgBr from GEM + Br, HgBr was oxidized by BrO, HO_2, OH, ClO, and IO to form Hg(II) brominated GOM species. However, under atmospheric conditions, the prevalent GEM oxidants in the MBL could be Br / BrO or O_3 / OH depending on Br and BrO mixing ratios. Relative humidity and products of the CH_3O_2 + BrO reaction possibly affected significantly the mixing ratios of Br or BrO radicals and subsequently GOM formation. Gas-particle partitioning could be potentially important in the production of GOM as well as Br and BrO at the marine site.

1 Introduction

Mercury (Hg) is a toxic pollutant found globally in air, natural waters, and soils. The health concern of Hg arises from the neurotoxic organic form, methyl mercury (MeHg), in the aquatic environments (Mason et al., 2006; Miller et al., 2007; Rolfhus et al., 2003). The high bioaccumulation and biomagnification of MeHg lead to human exposure through the consumption of seafood (Clarkson, 1994). Deposition of atmospheric Hg is one of the most important sources of aquatic Hg.

Title Page

Abstract | Introduction

Conclusions | References

Tables | Figures

|◀ | ▶|

◀ | ▶

Back | Close

Full Screen / Esc

Printer-friendly Version

Interactive Discussion

In the atmosphere, Hg exists in three forms: gaseous elemental mercury (GEM), gaseous oxidized mercury (GOM), and particulate bound mercury (PBM). The majority of atmospheric Hg is GEM, comprising $> 95\%$ of total gaseous mercury (TGM = GEM + GOM). The 0.8–1.7 years atmospheric lifetime of GEM is conducive to long range transport of Hg as a global pollutant (Bergan et al., 1999; Bergan and Rodhe, 2001; Holmes et al., 2006; Lin and Pehkonen, 1999; Schroeder and Munthe, 1998; Selin et al., 2007). In contrast, GOM and PBM are relatively short-lived and subject to dry and wet deposition due to their high solubility in water and low vapor pressure. GOM in the atmosphere can be produced from oxidation of GEM, released directly from anthropogenic emissions, and transformed from PBM. Oxidation of GEM was usually thought to be a major source of GOM in remote regions.

Chemical speciation of atmospheric Hg is essential to understand its geochemical cycle. Theoretical and experimental studies suggested that the main oxidants of GEM in the atmosphere are ozone (O_3), hydroxyl radical (OH), atomic bromine (Br), bromine monoxide (BrO), hydrogen peroxide (H_2O_2), and atomic chlorine (Cl), yielding GOM species of HgO, HgBrO, HgBr, Hg(OH)$_2$, HgCl, and through further reaction to other mercury halides (Ariya et al., 2015; Dibble et al., 2012; Lin and Pehkonen, 1999). Although efforts have been made to investigate the relative importance of these oxidants for GEM oxidation in the troposphere, it is still not well understood. In the terrestrial environment, it was suggested that the oxidation of GEM was primarily by O_3 and OH radicals (Shon et al., 2005; Sillman et al., 2007). In recent years, a consensus has emerged that the GEM + O_3 reaction most likely occurs with solid-phase products, whose speciation and quantification remain unknown (Ariya et al., 2015; Pal and Ariya, 2004b; Rutter et al., 2012; Snider et al., 2008). The reaction of GEM+OH has been subject to debate between theoretical and experimental studies, as no mechanism that is consistent with thermochemistry has been proposed (Ariya et al., 2015; Pal and Ariya, 2004a; Subir et al., 2011). In the MBL, measurements of GOM in the polar regions (Simpson et al., 2007; Steffen et al., 2008) to sub-tropical MBL (Laurier et al., 2003; Laurier and Mason, 2007; Obrist et al., 2011) and atmospheric mercury models

(Holmes et al., 2009, 2010; Kim et al., 2010; Lindberg et al., 2002; Obrist et al., 2011; Soerensen et al., 2010; Toyota et al., 2014; Wang et al., 2014; Xie et al., 2008) have also suggested Br as an important oxidant of GEM. The major source of atmospheric Br was suggested to be produced photolytically from Br-containing compounds and through the Br / BrO cycle involving tropospheric O_3 (Saiz-Lopez and Glasow, 2012; Simpson et al., 2015).

Hg chemistry in the MBL, the lowest part of the troposphere in direct contact with the sea surface, has global importance as approximately 70 % of the earth's surface is covered by oceans (Glasow et al., 2002). Hg in the MBL cycles differently from in coastal or inland areas. However, contemporary models are not able to reproduce GOM observations temporally and spatially due to knowledge gaps in Hg science, simplified model assumptions, and uncertainties of measurements (Ariya et al., 2015; Lin et al., 2006). In the polar region, bromine radicals were identified as the primary cause of the Arctic mercury depletion events (AMDE) (Kim et al., 2010; Lindberg et al., 2002; Toyota et al., 2014; Xie et al., 2008). In the MBL outside Polar Regions, due to lower mixing ratios of atmospheric halogen radicals, often lower than the detection limit, mechanisms for GOM production were more controversial than the Polar Regions. Using a box model, Hedgecock et al. (Hedgecock et al., 2003; Hedgecock and Pirrone, 2004, 2005) suggested that O_3 was a dominant GEM oxidant in the MBL at mid-latitudes in Mediterranean region, and that the GEM+O_3 reaction may form solid products. However, the reaction kinetics in their model were out-of-date with limited halogen chemistry, and fixed emission used in the model oversimplified the source terms. Holmes et al. (2009) simulated that GEM oxidation by Br comprised 35–60 % of the GOM sources using BrO concentrations calculated at a photostationary state from a prescribed distribution of Br mixing ratios. In this study a parameter was introduced to account for entrainment of free tropospheric GOM into the MBL and the Br mixing ratio was adjusted to capture the observed GOM diurnal trend, which could cause large uncertainties in GOM simulations. Most recently, Wang et al. (2014) employed updated Hg reactions together with bromine and iodine reactions, adopting the free tropospheric GOM entrainment

Title Page

Abstract | Introduction

Conclusions | References

Tables | Figures

◄ | ►

◄ | ►

Back | Close

Full Screen / Esc

Printer-friendly Version

Interactive Discussion

parameter from Holmes et al. (2009) for tropical MBL, and found Br to be a primary GEM oxidant, but oxidation by Br or O_3 / OH alone was unable to reproduce observed GOM concentration.

In this study, we employed a state-of-the-art chemical mechanism that incorporates gas and aqueous phase chemistry of Hg, O_3, and halogen to investigate the dynamics of GOM formation under various atmospheric conditions in mid-latitude regions. The most up-to-date kinetics was applied. Halogen radical mixing ratios (such as Br and BrO) were calculated using up-to-date atmospheric halogen reactions. Clear sky days with calm wind conditions were selected to minimize the entrainment effect of free tropospheric air and regional transport. Moreover, the initial GEM mixing ratios in the model were obtained from observations in three different environments and were set to be constant mimicking GEM emission flux.

2 Methods

2.1 Box model description

The Kinetic PreProcessor version 2.1 (Sandu and Sander, 2006) was utilized as the framework of the box model (Hedgecock et al., 2003; Hedgecock and Pirrone, 2004, 2005). A second order Rosenbrock method (Verwer et al., 1999) was applied to solve the coupled ordinary differential equations. The box model used in this study was initially set up by Kim et al. (2010). It was further improved in this study by incorporating the most up-to-date gas and aqueous phase chemical mechanisms (Atkinson et al., 2004; Dibble et al., 2012; Sander et al., 2011) to the model.

2.1.1 Reactions and kinetics

The box model has a total of 424 reactions: 276 gas-phase reactions (including Hg, halogen, O_3, sulfate, and hydrocarbon reactions), 52 gas-water equilibriums, 28 aqueous equilibriums and 68 aqueous reactions. Most of these reactions and kinetic data

were updated based on JPL Report No. 17 (Sander et al., 2011), Atkinson et al. (2004), and the references listed in Table 1. Photodissociation coefficients were calculated from the Tropospheric Ultraviolet and Visible (TUV) Radiation Model (Madronich, 1993).

The most important improvements in chemistry are gas and aerosol phase of Hg and halogen reactions. Gas-phase Hg reactions included in the box model are (Table 1):

1. Oxidation of GEM by O_3, OH, H_2O_2, Br, BrO, Cl, Cl_2, I (G1–8);

2. Reduction of HgBr to produce GEM (G9–11); and

3. Reactions of HgBr/HgCl with BrO, ClO, IO, NO_2, HO_2, and OH (G12–24) with kinetics suggested by Dibble et al. (2012).

Aqueous Hg reactions include:

1. Oxidations of Hg by O_3, OH, HOCl, and ClO^-, further oxidation of HgOH by O_2;

2. Reduction of Hg^{2+} by HO_2, photolytic reduction of $Hg(OH)_2$ and S(IV)-mediated reduction; and

3. Aqueous equilibria involving $HgSO_3$, $Hg(SO_3)_2^{2-}$, $HgOH^+$ and $Hg(OH)_2$. Gas-phase halogen reactions in the box model are mainly cycles of halogen radicals (Cl / Br / I and ClO / BrO / IO radicals).

The Cl / Br / I radical cycles include photodissociation of Cl_2 / Br_2/I_2, organic halides, and other inorganic halides as sources, and oxidation reactions as sinks. The ClO / BrO / IO radical cycles involve oxidation of Cl / Br / I radicals, photodissociation of $ClNO_2$ / $ClONO_2$ / $BrNO_2$ / $BrONO_2$, production from other halogen radicals, and sink reactions to reproduce Cl/Br/O radicals or other halides. Aqueous halogen reactions include reactions of Br^- / Cl^- and reactions of aqueous BrCl, HCl, HBr, HOCl, HOBr, Cl_2, and Br_2 species. The chemistry of halogen radicals, especially the reaction cycles of Br and BrO radicals, could be important and should not be neglected

or replaced by simple approximation as previous Hg box model studies outside of Polar regions did. Hence, the most up-to-date halogen chemistry from the literature was included in our model.

2.1.2 Initial conditions and input data

Observations at three sites from the University of New Hampshire (UNH) AIRMAP Observing Network (http://www.eos.unh.edu/observatories/data.shtml) were used: a marine site located on Appledore Island (AI) in the Gulf of Maine (42.97° N, 70.62° W, 40 m a.s.l.), a coastal site located in Thompson Farm (TF) in Durham, NH (43.11° N, 70.95° W, 24 m a.s.l.), and an inland site located on Pack Monadnock (PM) in Miller State Park in Peterborough, NH (42.86° N, 71.88° W, 700 m a.s.l.) (Fig. 1). Hourly mean values of GEM, O_3, CO, NO, meteorological observations (i.e., temperature, relative humidity, wind speed, and solar radiation) at these three sites were used as initial input to the box model. Observations of GOM mixing ratios from the three sites were utilized to evaluate the model performance. GEM and GOM data were collected using the Tekran[®] 2537/1130/1135 unit (Tekran Inc., Canada). Detailed information on these measurements can be found in Mao and Talbot (2004), Talbot et al. (2005), Fischer et al. (2007), Mao et al. (2008), and Sigler et al. (2009). Table 2 lists the input variables of the box model. The model's initial mixing ratios of GEM, O_3, CO, and NO were obtained from observations and were set to be constant during a simulation. Dry deposition flux was calculated using dry deposition velocity data derived from Zhang et al. (2009, 2012) and boundary layer height estimated from Mao and Talbot (2004). Other physical parameters (i.e. Henry's constants, liquid water content, and aerosol radius) were used to simulate the gas-particle partitioning process in the box model.

7

Title Page

Abstract | Introduction

Conclusions | References

Tables | Figures

◄◄ | ►►

◄ | ►

Back | Close

Full Screen / Esc

Printer-friendly Version

Interactive Discussion

2.1.3 Gas-particle partitioning

An empirical expression was utilized to calculate particle size growth relative to its dry radius (r_{dry}) (Lewis and Schwartz, 2006):

$$r = r_{dry}\frac{4}{3.7}\left(\frac{2-RH}{1-RH}\right)^{1/3}, \tag{1}$$

where RH is the relative humidity, and r is the particle radius at RH.

Gas-particle partitioning was treated by mass transfer between droplets and air. The dynamic mass transfer coefficient across the gas–aqueous interface was calculated using the method developed by Schwartz (1986). The net mass flux (F, molecule $cm^{-3}\,s^{-1}$) between the gas and aqueous phase is given by

$$F = k_{mt} \times \left(L \times c_g - \frac{c_{aq}}{HRT}\right), \tag{2}$$

where L is the liquid water content ($m^3_{water}\,m^{-3}_{air}$), k_{mt} is the mass transfer coefficient (s^{-1}), c_g is the gas phase concentration of the species (molecules cm^{-3}), c_{aq} is the aqueous phase concentration of species (molecules cm^{-3}), H is the Henry's constant of the species ($M\,atm^{-1}$), R is the universal gas constant ($atm\,L\,K^{-1}\,mol^{-1}$), and T is atmospheric temperature (K). k_{mt} is calculated as follow:

$$k_{mt} = \left(\frac{r^2}{3D_g} + \frac{4r}{3\overline{v}\alpha}\right)^{-1}, \tag{3}$$

$$\overline{v} = (8RT/M\pi)^{1/2}, \tag{4}$$

where r is the particle radius (μm), D_g is the diffusion coefficient ($m^2\,s^{-1}$), $\overline{v}$ is the mean thermal molecular velocity ($m\,s^{-1}$), α is the dimensionless accommodation coefficient, and M is the species molecular weight ($g\,mol^{-1}$).

Title Page

Abstract | Introduction

Conclusions | References

Tables | Figures

⏮ | ⏭

◀ | ▶

Back | Close

Full Screen / Esc

Printer-friendly Version

Interactive Discussion

2.2 Case selection

A total of 83 cases were examined to investigate the role of chemistry in Hg cycling in the MBL, coastal, and inland environments. At the study sites, significant warm season declines of GEM were observed with annual maximums in spring and minimums in

5 autumn resulting in seasonal amplitudes up to 100 ppqv at TF (Mao et al., 2008). The lost GEM during the warm season most likely entered the ecosystem. Chemical transformation of GEM in warm seasons was suspected to be one of the factors causing the observed seasonal decline in GEM. As such, this study selected the cases representing summer days when chemical processes were most likely dominant. To exclude the

10 influence of wet deposition, we selected clear-sky conditions based on the observed photodissociation rate constant of NO_2 (jNO_2) and solar radiation flux. To minimize the influence of transport, cases with arithmetic daily mean wind speed higher than 75 % percentile of all summer days in studied years ($> 1.3\,\mathrm{m\,s^{-1}}$ at TF, $> 6\,\mathrm{m\,s^{-1}}$ at PM, and $> 7\,\mathrm{m\,s^{-1}}$ at AI) were excluded. As a result, 50, 12, and 21 clear-sky days at

15 AI (marine), TF (coastal), and PM (inland, elevated), respectively, were selected from summers of 2007, 2008, and 2010. Since there was no temperature data available for summer 2009 at TF, 2009 was not considered.

2.3 Backward trajectory model

The National Oceanic and Atmospheric Administration (NOAA) Hybrid Single Parti-

20 cle Lagrangian Integrated Trajectory (HYSPLIT) trajectory model was used to identify source regions of air masses at the three sites. The model runs were performed over twenty-four hours using the NOAA NAM (Eta) Data Assimilation System (EDAS) data with a 40 km × 40 km horizontal resolution as input. Backward trajectories and trajectory clusters were calculated.

2.4 Model evaluation

To evaluate the box model performance with observations, the following statistical performance measures (Chang and Hanna, 2004; Hanna, 1988; Hanna et al., 1991, 1993), which include the functional bias (FB), the normalized mean square error (NMSE), the root mean square error (RMSE), and the partition of NMSE due to systematic errors (NMSE$_s$) were used:

$$FB = \left(\overline{C_0} - \overline{C_p}\right) / 0.5\left(\overline{C_0} + \overline{C_p}\right), \tag{5}$$

$$NMSE = \overline{\left(C_0 - C_p\right)^2} / \overline{C_0 C_p}, \tag{6}$$

$$RMSE = \sqrt{\overline{\left(C_0 - C_p\right)^2}}, \tag{7}$$

$$NMSE_s = 4FB^2 / (4 - FB^2), \tag{8}$$

where C_p is model predictions, C_0 is observations, overbar $(\overline{C})$ is average over the dataset.

3 Results and discussion

3.1 General characteristics in measured GOM and GEM

In the selected 83 cases, atmospheric GOM and GEM mixing ratios varied greatly at the three sites (Fig. 2). Mixing ratios of GOM varied over 0.03–87.79 ppqv at AI, 0.04–4.93 ppqv at TF, and 0–0.65 ppqv at PM. GOM did not show consistent diurnal variation at these sites. At AI and TF, significant diurnal variation was observed with afternoon maximums and nighttime minimums. At AI, GOM peaked at 10 ppqv over 14:00–16:00 EDT and was ∼ 5 ppqv at night, well above the limit of detection (LOD, ∼ 0.1 ppqv, from Sigler et al., 2009). At TF, GOM mixing ratios peaked at 0.75 ppqv at

10

17:00 EDT and were below LOD at night, before 08:00 EDT. The GOM diurnal cycle at PM was different from that at AI and TF. At PM, averaged GOM had higher mixing ratios at night and in the early morning than in the afternoon. However, the median values were showing afternoon peaks and nighttime minimums. The difference between aver-

5 age and median GOM diurnal cycles was driven by 3 cases that had abnormally high GOM mixing ratios (> 0.6 ppqv) at night or in the early morning relative to the average GOM mixing ratio through the day (~ 0.1 ppqv).

Mixing ratios of GEM ranged over 65–231 ppqv at AI, 60–213 ppqv at TF, and 121–231 ppqv at PM (Fig. 2). On average, GEM mixing ratios at PM were 8 % higher than

10 that at TF and 12 % higher than that at AI. Unlike GOM, GEM diurnal cycles showed nearly flat patterns at AI and PM, though slightly higher (~ 3 %) GEM mixing ratios at night than in the daytime were observed at PM. In contrast, the average GEM diurnal cycle at TF showed an early morning (07:00 EDT) minimum (112 ppqv) and a daytime (13:00 EDT) maximum (153 ppqv).

15 The site differences of GOM and GEM diurnal cycles could be attributed to different chemical environments, land surface types, and meteorological conditions. For example, the GEM daily minimum at night and in the early morning at TF was likely caused by a strong net loss dominated by dry deposition under nocturnal inversion (Mao et al., 2008; Mao and Talbot, 2012). Nocturnal inversion also influenced the GEM and GOM

20 diurnal cycles at PM, albeit differently from at TF. The elevation of PM site is 700 m a.s.l., above the nocturnal inversion layer (< 200 m) (e.g. Kutsher et al., 2012), and thus GEM and GOM at night were continuously replenished by those produced from daytime and remaining in the residual layer, which likely caused higher nighttime values at PM. Daytime peaks of GOM at TF and AI were most likely caused by photochemical oxidation

25 of GEM under strong solar radiation. The causes for such variation were examined in Sect. 3.2.2.

Title Page

Abstract | Introduction

Conclusions | References

Tables | Figures

◄ | ►

◄ | ►

Back | Close

Full Screen / Esc

Printer-friendly Version

Interactive Discussion

3.2 Simulated diurnal variation and speciation of GOM

Model simulated diurnal cycles of GOM averaged over the 50, 12, and 21 clear-sky days at AI, TF, and PM, respectively, were shown in Fig. 3. The patterns of diurnal variation were similar at the three sites with daily peaks at $\sim$ 14:00 LT, but the magnitude varied by site. AI had the largest GOM diurnal amplitude (i.e., daily maximum – daily minimum) ranging from 0.45 to 20.99 ppqv, TF from 0.02 to 1.85 ppqv, and PM showed negligible diurnal variation. Similar magnitude variation was also exhibited in GOM observations (Fig. 2). Overall, simulated GOM mixing ratios at the three sites were in agreement with observations (detailed comparison in Sect. 3.4).

The simulations suggested that the dominant GOM species and GEM oxidants varied by site (Fig. 4). At AI, brominated GOM species comprised 50–71 % of the total GOM over 09:00–16:00 EDT, whereas HgO was dominant (56–92 % of the total GOM) during the remaining day. At TF and PM, HgO was the predominant GOM species (80–99 %). HgO was produced from oxidation of GEM by O_3 and OH. The contribution to HgO from oxidation by O_3 was larger than by OH except at noon when OH mixing ratios reach daily peaks resulting in comparable contributions (48 and 52 % by OH and O_3, respectively). At AI, HgBrO, BrHgOOH, and BrHgOBr were the most abundant brominated GOM species, which constituted $\sim$ 99 % of the total brominated GOM. HgBrO was produced from the GEM + BrO reaction, while BrHgOOH and BrHgOBr were produced from GEM oxidation by Br radicals followed by reactions of HgBr with HO_2 and BrO. $Hg(OH)_2$ from GEM oxidation by H_2O_2 appeared to be an important nighttime GOM species at the inland site (PM), accounting for 33 % of the total GOM at night. Other GOM species were negligible in the studied cases.

Title Page

Abstract | Introduction

Conclusions | References

Tables | Figures

|◄ | ►|

◄ | ►

Back | Close

Full Screen / Esc

Printer-friendly Version

Interactive Discussion

3.3 Sensitivity analysis

3.3.1 Sensitivity of GOM to physical and chemical parameters

The base case (Case 0) of these sensitivity runs represented the real atmospheric conditions on the selected 50 days at AI. Case 1–10 are sensitivity cases where one parameter in the base case was changed (Table 3). Case 1 turned off photolysis reactions. Cases 2–4 tested the gas-particle partitioning scheme. Cases 5–8 tested the sensitivity of GOM mixing ratios to GEM oxidation reactions and their coefficients. Cases 9–10 tested the sensitivity of GOM mixing ratios to temperature.

The importance of photochemical radicals in GEM oxidation was demonstrated clearly in decreases of 21–80 and 28–92 % in daytime GOM and PBM, respectively with largest decreases at noon as a result of turning off photochemistry (*Case 1*). *Case 2* showed ~ 74 % of oxidized Hg transformed to PBM at AI with gas-particle partitioning switched on. In this case, HgO and Hg(OH)$_2$ were more sensitive than halogenated GOM species (such as BrHgOOH and BrHgOBr). Turning off gas-particle partitioning more than quadrupled the mixing ratios of HgO and Hg(OH)$_2$ throughout the day compared to increases of more than 100 and 60 % halogenated GOM species during daytime and nighttime, respectively.

Decreasing liquid water content by 1 order of magnitude tripled GOM mixing ratios, whereas increasing the same amount decreased GOM by 87 % (*Cases 3–4*). Sensitivity of GOM and PBM mixing ratios to dominant GEM oxidation reactions are shown in *Cases 5–8*. Using the slowest rate coefficient of GEM + O$_3$ obtained from Hall (1995), as opposed to the one from Snider et al. (2008) led to a decrease of 56.7 % in HgO, and decreases of 15 and 85 % in total GOM during daytime and nighttime, respectively. Turning off GEM oxidation by O$_3$, OH, or Br resulted in decreases of 19, 10, and 30 %, respectively, in daytime GOM mixing ratios. Turning off the GEM + Br oxidation reaction also decreased daytime PBM mixing ratios by 45 %. However, for nighttime GOM and PBM mixing ratios, turning off the GEM + O$_3$ reaction caused decreases of 92 and

5 %, respectively, since Br and OH are both photochemical radicals and O_3 was the predominant oxidant for GEM in the model.

Cases 9–10 suggested that nighttime GOM and PBM mixing ratios were more sensitive to temperature than those during daytime. Increasing temperature by 10 K caused a 9 % increase each in GOM and PBM mixing ratios during daytime but a decrease of 13 % in GOM and 54 % in PBM at night. This was because the rate coefficient of GEM + O_3 increases with increasing temperature, but the rate coefficient of GEM + OH decreases with increasing temperature.

3.3.2 Influence of physical and chemical processes on GOM diurnal cycle

Large variations were exhibited in both observed (Fig. 2) and simulated (Fig. 3) GOM mixing ratios at AI, TF, and PM. Considering that all cases were under relatively calm, clear-sky conditions, the simulated GOM mixing ratio and diurnal cycle were controlled primarily by chemical reactions, dry deposition, and gas-particle partitioning. To quantify the contribution of processes to the difference of GOM mixing ratios at the three sites, three sensitivity cases were conducted at TF and PM: (1) use the same dry deposition velocity and boundary layer height as those of AI for TF (denoted as TF_AIdry) and PM (denoted as PM_AIdry), (2) use the same gas-particle partitioning parameters as those of AI for TF (denoted as TF_AIaero) and PM (denoted as PM_AIaero), (3) use the same physical parameters as those of AI for TF (denoted as TF_AIaerodry) and PM (denoted as PM_AIaerodry).

Comparison of simulated GOM diurnal cycles from the AI, TF_AIaerodry and PM_AIaerodry cases showed the influence of different chemical scenarios on GOM mixing ratios at the three sites. At night, GOM mixing ratios at the three sites did not vary significantly (0–2 ppqv), with higher values at PM than those at AI and TF (Fig. 5). However, the mid-day peak at AI was more than one order of magnitude higher than those in the PM_AIaerodry and TF_AIaerodry cases, indicating more chemical transformation of Hg occurring at AI. The daytime mixing ratios of GOM at TF and PM were similar, while the nighttime GOM mixing ratios at PM were 30–52 % higher than at AI

Title Page

Abstract	Introduction
Conclusions	References
Tables	Figures

|◄ | ►|

| ◄ | ► |

| Back | Close |

Full Screen / Esc

Printer-friendly Version

Interactive Discussion

and 20–200 % higher than at TF. This probably resulted from larger nighttime GEM and O_3 mixing ratios, hence producing more GOM, at PM than those at TF and AI. Specifically, nighttime GEM mixing ratios at PM were 8–15 % higher than at AI and 8–34 % higher than TF cases, while nighttime O_3 mixing ratios at PM were 11–70 % larger than at AI and 35–260 % larger than at TF. PM had higher nighttime GEM and O_3 mixing ratios, because this site was exposed in the residual boundary layer at night due to its high elevation, constantly replenished with the regional pool of air from daytime. Overall, chemical transformation contributed $\sim$ 60 % of the daytime difference in GOM between AI and the two sites over land (TF and PM), 33 % of the nighttime difference between AI and TF, and 26 % of the difference between PM and AI.

Dry deposition and gas-particle partitioning contributed 4–37 and 30–96 %, respectively of the total GOM difference between AI and PM. Both processes had larger contributions at night that during daytime. Dry deposition contributed 6–24 % of the GOM difference between AI and TF and gas-particle partitioning 18–78 %.

3.3.3 Br chemistry in the MBL

Diurnal cycles of Br and BrO radicals (Fig. 6) were simulated using the Br chemical mechanism described in Sect. 2. Photodissociation of Br_2 was the main source of Br and BrO radicals during daytime. Our simulations suggested that reactive Br compounds were significant gaseous oxidants of GEM in the MBL at a fixed initial mixing ratio of 5.6 ppqv for Br_2. Increasing initial mixing ratios of Br_2 by 25 % resulted in an increase of 0.01–2.15 ppqv in GOM mixing ratios.

In addition, the reaction of BrO with methyldioxy (CH_3O_2) radicals could have important influence on the mixing ratios of Br, BrO, and GOM. Simulated daytime mixing ratios of CH_3O_2 was $\sim$ 40 pptv, and the rate coefficient of $(5.7 \pm 0.6) \times 10^{-12}$ cm^3 molecule^{-1} s^{-1} at 298 K for $BrO + CH_3O_2$ (Aranda et al., 1997a) was used for our simulations. Pathways B1, B2, and B3 were suggested by Aranda et al. (1997a) based on an experimental study (Table 4). However, the production of CH_3O may be due to its self-reaction in B1. Guha and Francisco (2003) suggested CH_3OOOBr

to be a likely intermediate of this reaction, and that CH_3OOOBr could dissociate to $CH_2O + HOOBr$ (B4, Table 4). Based on thermodynamics calculations, CH_3OBr and O_2 (B3, Table 4) were possible products. BrOO and HOBr were both included in the Br chemical cycle and can be transformed back to Br and BrO radicals in the model.

5 However, it is unclear whether CH_3OBr (product of B3) or HOOBr (product of B4) could be transformed back to Br and BrO radicals in the atmosphere. In this case, using the B3 or B4 pathway did not appear to make a difference in our box model results.

In this study, the B1 and B2 pathways were used for the $CH_3O_2 + BrO$ reaction as part of the *base case* simulation (denoted as Sim-avg BrOO). The sensitivity case

10 Sim-avg CH_3OBr used the B3 pathway in lieu of B1 and B2. The simulated average and the range of GOM diurnal cycles in the base case and the sensitivity case were evaluated against observed mean and median GOM diurnal cycles of the 50 study cases at AI (Fig. 7). If the $CH_3O_2 + BrO$ reaction followed the B1 and B2 pathways, this reaction had a negligible effect on reactive Br radicals. However, if B3 or B4 was

15 applied, the simulated total GOM mixing ratio was lowered by 50 % during daytime. Moreover, the simulated GOM diurnal cycle in the base case agreed favorably with the observed *average* GOM diurnal cycle (NMSE = 15 %), while the results of the Sim-avg CH_3OBr case were in better agreement with the observed *median* GOM diurnal cycle (NMSE = 14 %). These agreements indicated that, if the $BrO + CH_3O_2$ reaction was

20 a net sink of BrO radicals, the model was able to simulate better most cases, whereas if the product of $BrO + CH_3O_2$ was transformed back to Br or BrO radicals, the model appeared to capture those cases with large GOM mixing ratios (> 6 ppqv). Due to the scarcity of kinetic research on the B3 and B4 pathways, we used B1 and B2 pathways for $CH_3O_2 + BrO$ reaction in this study.

25 In summary, the pathways of $BrO + CH_3O_2$ could play an important role in atmospheric Br chemistry and Hg speciation in Br-rich environments. Research on the reaction pathways and rate coefficients of the $BrO + CH_3O_2$ reaction is warranted to better assess the role of this reaction.

Title Page

Abstract	Introduction
Conclusions	References
Tables	Figures

◄◄	►►
◄	►
Back	Close

Full Screen / Esc

Printer-friendly Version

Interactive Discussion

(cc) BY

3.4 Model evaluation

For all cases at AI and TF, the average simulated and observed GOM diurnal cycles agreed reasonably well in both magnitude and shape, whereas at PM the model appeared to have missed both (Fig. 8). Three salient features were noted for the disagreement between the model and observational results. First, standard deviation from observations was a factor of 2–7 larger than the simulated. This suggested that the model could capture the mean values of GOM, but not the very low and very large mixing ratios. Second, observed nighttime GOM mixing ratios were 12–200 % larger than the simulated at AI, indicating that the model did not capture certain nighttime processes producing GOM in the marine boundary layer. Third, the simulated diurnal cycle was the opposite of the observed at PM, with the maximum during the day and minimum at night. It was likely that the model simply simulated the dependence of GOM production on solar radiation. At PM, more processes contributed to the diurnal variation. At night, the site is above the nocturnal boundary layer and exposed to the GOM produced from the daytime, which could continually replenish surface GOM at the site that was lost via dry deposition and perhaps reduction. The model-observation discrepancies for the three sites were discussed as follows.

3.4.1 Appledore Island (marine)

Of the 50 cases at AI, 27 diurnal cycles of GOM were simulated with the average values and patterns close to the observed and $NMSE_s = 2.86$ %, denoted as *matching* cases hereafter, 8 were underestimated with $NMSE_s = 146$ %, and 15 were overestimated with $NMSE_s = 167$ %. The observed and simulated average GOM mixing ratios and the corresponding ranges were calculated for the matching, under-estimation, and over-estimation cases at AI (Fig. 9a). For more than half of the time (27 matching cases out of 50 cases in total), the model captured the average GOM diurnal cycle, the diurnal cycle pattern and overall GOM levels. Beyond that, Fig. 9a shows large difference in the observed GOM levels among the matching, under-estimation, and over-estimation

cases. On average, the observed daytime peak in the under-estimation cases was about twice as large as that for the matching cases and 7 times larger than that for the over-estimation cases. However, such difference was not captured by the model, suggesting that one or more GOM producing processes in the MBL were not included or not realistically represented in the box model. In addition, the GOM diurnal pattern of the over-estimation cases was different from those in the under-estimation and matching cases. The average observed GOM diurnal cycles of the under-estimation and matching cases both exhibited a daily maximum at 13:00 EDT and a minimum over 04:00–08:00 EDT whereas for the over-estimation cases a daily maximum at around 20:00 EDT and a minimum at 07:00–08:00 EDT.

Such differences were caused possibly by the challenges of simulating Br and BrO in the MBL at AI. No measurements of Br and BrO radicals as well as Br_2 were available at AI. To reasonably simulate mixing ratios of Br and BrO, Br_2 mixing ratios were calculated based on the BrO observations at a mid-latitude MBL site from Saiz-Lopez et al. (2006), which was ~ 5.6 ppqv during the daytime (06:00–21:00 EDT). Saiz-Lopez et al. (2006) showed that the daytime peak mixing ratios of BrO in the MBL could vary by a factor of 2 over a time period of 3 days. Such variation was not captured in our box model, which could result in uncertainty of up to 100 % in simulated Br mixing ratios with subsequent effects on GOM simulation.

In the over-estimation cases, the simulated GOM daytime peaks were very low, and appeared later during the day than in the under-estimation and matching cases. Considering the late afternoon peak (17:00 EDT) of O_3 compared to the noontime peak of Br radicals, O_3 possibly played a more important role in the over-estimation cases. To verify this hypothesis, a sensitivity simulation was conducted without the initial Br_2 mixing ratio fixed for these cases, termed as the O_3 / OH case. In this case, the Br_2 concentration rapidly diminished with time and consequently the concentrations of Br and BrO were very low. The O_3 / OH case turned out to better represent these 15 over-estimation cases with $NMSE_s$ = 34 % (compared to 167 % with Br_2 mixing ratio fixed).

18

This suggested that in the MBL, Br may be a dominant GEM oxidation most of the time, but occasionally at low Br mixing ratios, O_3 could become dominant.

To identify the potential sources of GOM at AI, backward trajectory analysis was conducted using the HYSPLIT4 model (https://ready.arl.noaa.gov/HYSPLIT.php). All 24 h backward trajectories started from the time of GOM daily peaks for the 50 cases. The trajectory results were clustered for over-estimation, matching, and under-estimation cases (Fig. 10). Based on these trajectories, in about half of the 15 over-estimation cases air masses originated from marine environments, while in more than 80 % of the 27 matching cases and 7 out of 8 under-estimation cases air masses came from inland northwest of AI. Note that in those under-estimation cases GOM mixing ratios were exceptionally large, exceeding 30 ppqv.

Different source areas of air masses reaching AI could be one of the reasons for the large variation of GOM observations. The highest levels of GOM were observed in summer with RH roughly < 50 % at AI (Mao et al., 2012). A close examination of the 50 cases at AI revealed low RH levels ($\leq$ 45 %) on 16 days. The time periods with RH $\leq$ 45 % appeared mostly (78 % of the time) in the afternoon over 12:00–20:00 EDT and less so (22 %) at night over 21:00–02:00 EDT. During these time periods, increased GOM (15 out of 16, compared with periods with high RH on the same day) and daily maximum GOM (10 out of 16) occurred simultaneously at low RH, regardless of the time of the day.

Interestingly, the RH level of 45 % corresponds to the crystallization point of NaCl (Cziczo et al., 1997; Tang et al., 1997). The crystallization of sea-salt aerosols might be link to the very high GOM peaks in certain ways. Rutter and Schauer (2007) found that particles of potassium and sodium chlorides had high partitioning coefficients that could shift the GOM gas-particle partitioning toward the aqueous phase, while ammonium sulfate, levoglucosan, and adipic acid would shift the partitioning toward the gas phase. It was thus *hypothesized* that certain processes might have been activated during transport of inland air masses to the MBL involving the interaction between land and marine air, which potentially resulted in those very high GOM mixing ratios.

Laskin et al. (2012) found effective reactivity of chloride (Cl^-) components with organic acid in sea salt aerosols (SSAs), possibly leading to depletion of Cl^- and formation of organic salts in aerosols. Biogenic compounds in air masses originating from inland forested areas could be oxidized forming organic acids in transit. As inland air reached the MBL, these organic acids would deposit onto SSAs and could subsequently change SSAs' chemical and physical properties, such as lowering concentrations of Cl^- and forming a thick organic film on the outside of SSAs. The lower concentrations of Cl^- and higher concentrations of organic acid in aerosols might have contributed to the shift in the gas-to-particle partitioning to the gas phase and resulted in higher GOM mixing ratios in the atmosphere.

Another possible explanation could be air masses of inland origin encountering marine air rich in atmospheric Br and BrO radicals. The main source of atmospheric Br is thought to come from the release of Br_2 and BrCl from SSA (Finlayson-Pitts, 2010; Sander et al., 2003). Experimental studies suggested Br^- enhancements of a factor of 40 to 140 on the surface of sufficiently dry artificial SSA (Ghosal et al., 2008; Hess et al., 2007). Therefore, when drier inland air masses were mixed with marine air in the MBL under relatively low RH conditions, SSA became drier, forcing more Br_2 to be released from SSA, resulting in enhanced oxidation of GEM by Br and BrO radicals. These hypotheses need to be validated in future research. These mechanisms are presently missing in the box model, leading to the model's inability to capture very high GOM mixing ratios. Measurements of halogen species and a better gas-particle partitioning mechanism are needed to better the model's performance.

3.4.2 Thompson Farm (coastal)

Generally, the box model performed well at TF (Fig. 8b) with overall $NMSE_s = 0.75\%$ and $RMSE = 0.78$ ppqv. Of the 12 cases at TF, 7 diurnal cycles of GOM (58 %) were simulated reasonably well with $NMSE_s < 50\%$, only one was underestimated by $\sim 70\%$, and 4 cases were overestimated by a factor of 3 to 6. Overall, the observed average diurnal cycles of GOM for all selected summer clear-sky days at TF

had daily peaks during 14:00–20:00 EDT with very low values at night between 0:00 and 8:00 EDT (Sigler et al., 2009) (Fig. 8b). The peak observed at 17:00 EDT (Fig. 8b) was largely affected by the abnormally high GOM peak in that one under-estimation case (Fig. 9b).

5   For the over-estimation and matching cases, the model reproduced very low GOM mixing ratios at night (Fig. 9b). For the same reason substantially lowering GEM mixing ratios at night and in the early morning at TF (Mao et al., 2008), the low nighttime GOM at TF was probably caused by loss via dry deposition under nocturnal inversion. To capture these low values in model simulations, realistic nocturnal boundary layer height

10   data were needed beside solid representation of dry deposition and chemistry in the model. The diurnal cycle of boundary layer height in the box model was parameterized based on reanalysis data obtained from the Research Data Archive at the National Center for Atmospheric Research (http://rda.ucar.edu/datasets/ds093.0/). Use of these data helped to reproduce the low nighttime GOM levels in simulations for the TF site.

15   Another notable feature in Fig. 9b is the exceedingly high observed GOM mixing ratios in the sole under-estimation case and the low observed GOM mixing ratios throughout the day in all over-estimation cases. Observed GOM mixing ratios in the under-estimation case showed a factor of 3–7 larger than those in the matching cases, and a factor of 3–31 larger than those in the over-estimation cases (Fig. 9b). Concur-

20   rently, larger fine particle concentrations, $8272\,\mathrm{cm^{-3}}$ on average, were observed for the under-estimation case, which was 65 and 93 % larger than those in the matching cases and over-estimation cases, respectively. Lower RH, 59 % on average, was observed in the under-estimation case, 11 and 15 % lower than that in the matching and over-estimation cases, respectively. Moreover, higher air pressure (1017, 7 and 10 hPa

25   larger than the matching and over-estimation cases, respectively), lower wind speed ($0.59\,\mathrm{m\,s^{-1}}$ on average, 47 and 56 % lower than matching and over-estimation cases respectively), and stronger solar radiation flux (8 and 13 % stronger than matching and over-estimation cases respectively) were found in the under-estimation case. Clearly, the under-estimation case occurred under the strongest Bermuda High influence, with

Title Page

Abstract | Introduction

Conclusions | References

Tables | Figures

◀ | ▶|

◀ | ▶

Back | Close

Full Screen / Esc

Printer-friendly Version

Interactive Discussion

the calmest, sunniest, and driest conditions of all cases, which is most conducive to photochemistry and pollution build-up that may have ultimately contributed to the very large GOM mixing ratios in that one under-estimation case. Our model appeared to fail to mimic the chemistry under such conditions that produced the largest GOM mixing ratios.

3.4.3 Pack Monadnock (inland, rural, elevated site)

At PM, diurnal cycles of GOM were overestimated with $NMSE_s = 70\%$ and overall RMSE = 0.13 ppqv. However, considering the extremely low mixing ratios of GOM observed at PM (Fig. 2), cases with RMSE < 0.1 ppqv (LOD) were considered as matching cases. Therefore, the model reasonably simulated 11 out of 21 (52 %) cases, underestimated in 3, and overestimated in 7. Evaluation of simulated GOM diurnal cycles against observations (Fig. 8c) showed reasonable agreement with general overestimation ranging over 0.05–0.07 ppqv.

The observed GOM diurnal cycle (Fig. 8c) showed daily maximums at 08:00 and 23:00 EDT, which were mainly influenced by the three underestimated cases (Fig. 9c). In comparison, rest (86 %) of the cases were showing a very flat pattern of GOM diurnal cycle at PM. The first and the most important reason for such observation-model discrepancy is that the PM site is a mountain site (700 m a.s.l.), which is above the nocturnal inversion layer ($\sim$ 200 m at TF) at night but in the middle of the convective boundary layer during the day. At night, a regional pool of GOM produced during daytime remained in the residual layer, which kept the surface GOM levels from dropping below the LOD at night at PM. The slight decline of GOM mixing ratios after sunrise was because of mixing with the lower altitude air masses with depleted GOM from the night. The effect of the PM's site characteristics was not represented in the box model, which could result in model's inability to simulate diurnal variation associated with this aspect of the site. In addition, due to the dominance of GEM oxidation by O_3 in GOM production in the model, it was highly likely that the flat patterns (slightly higher at night) of GEM (Fig. 2) and O_3 were mirrored in GOM mixing ratios.

4 Summary

This study provided a state-of-the-art chemical mechanism for atmospheric Hg model-
ing system and tested the chemical mechanism for three different environments using
a mercury box model. Eighty-three summer clear-sky days were selected at marine,
coastal, and inland elevated sites in southern New Hampshire to evaluate the model.
As a result, for each of the three environments, GOM diurnal cycles of over half se-
lected cases were reasonably represented by the box model. It was hypothesized that
dry air masses with organic compounds transported from inland may result in very
large GOM mixing ratios in the MBL possibly due to changing physical and chemical
properties of sea salt aerosols. The low nighttime and morning GOM mixing ratios at
coastal site were likely a result of a net loss due to dry deposition in the nocturnal inver-
sion layer. The GOM mixing ratios above the limit of detection at the inland site at night
were probably caused by constant replenishment from a regional pool, in the residual
boundary layer, of GOM that was produced in the daytime convective boundary layer.
The updated chemical mechanism largely improved GOM diurnal cycle simulations
at the coastal and inland sites. HgO produced from oxidation of GEM by O_3 and OH
dominated GOM species at the coastal and inland sites, while bromine-induced mer-
cury species (mainly BrHgOOH, BrHgOBr, and HgBrO) were important at the marine
site. In Br chemistry, the products of the $CH_3O_2 + BrO$ reaction strongly influenced the
simulated Br and Hg concentrations. In this study, GEM oxidation by O_3 and OH was
represented in ways similar to those in regional and global models, which is limited
by the current nebulous understanding of potential surface chemistry. It should also be
acknowledged that studies have suggested problems in GOM measurements using the
current Tekran instruments (Gustin et al., 2015; Jaffe et al., 2014). If indeed real atmo-
spheric GOM concentrations were underestimated in Tekran measurements, it implies
even more confounding, yet unknown issues in our current understanding of Hg chem-
istry. More experimental or theoretical studies on Hg reactions and better GOM mea-
surement data are warranted to improve our understanding and subsequently model

simulations of atmospheric Hg cycling, which can ultimately serve policy-making in an effective manner.

References

Aranda, A., Le Bras, G., La Verdet, G., and Poulet, G.: The BrO + CH$_3$O$_2$ reaction: kinetics and role in the atmospheric ozone budget, Geophys. Res. Lett., 24, 2745–2748, 1997.

Ariya, P. A., Khalizov, A., and Gidas, A.: Reactions of gaseous mercury with atomic and molecular halogens: kinetics, product studies, and atmospheric implications, J. Phys. Chem. A, 106, 7310–7320, 2002.

Ariya, P. A., Amyot, M., Dastoor, A., Deeds, D., Feinberg, A., Kos, G., Poulain, A., Ryjkov, A., Semeniuk, K., Subir, M., and Toyota, K.: Mercury physicochemical and biogeochemical transformation in the atmosphere and at atmospheric interfaces: a review and future directions, Chem. Rev., 115, 3760–3802, doi:10.1021/cr500667e, 2015.

Atkinson, R., Baulch, D. L., Cox, R. A., Crowley, J. N., Hampson, R. F., Hynes, R. G., Jenkin, M. E., Rossi, M. J., and Troe, J.: Evaluated kinetic and photochemical data for atmospheric chemistry: Volume I – gas phase reactions of O$_x$, HO$_x$, NO$_x$ and SO$_x$ species, Atmos. Chem. Phys., 4, 1461–1738, doi:10.5194/acp-4-1461-2004, 2004.

Atkinson, R., Baulch, D. L., Cox, R. A., Crowley, J. N., Hampson, R. F., Hynes, R. G., Jenkin, M. E., Rossi, M. J., Troe, J., and Wallington, T. J.: Evaluated kinetic and photochemical data for atmospheric chemistry: Volume IV – gas phase reactions of organic halogen species, Atmos. Chem. Phys., 8, 4141–4496, doi:10.5194/acp-8-4141-2008, 2008.

Balabanov, N. B., Shepler, B. C., and Peterson, K. A.: Accurate global potential energy surface and reaction dynamics for the ground state of HgBr$_2$, J. Phys. Chem. A, 109, 8765–8773, 2005.

Baumgardner, D., Raga, G. B., Kok, G., Ogren, J., Rosas, I., Báez, A., and Novakov, T.: On the evolution of aerosol properties at a mountain site above Mexico City, J. Geophys. Res.-Atmos., 105, 22243–22253, doi:10.1029/2000JD900299, 2000.

Bergan, T. and Rodhe, H.: Oxidation of elemental mercury in the atmosphere; constraints imposed by global scale modelling, J. Atmos. Chem., 40, 191–212, 2001.

Title Page

Abstract	Introduction
Conclusions	References
Tables	Figures

|◄ | ►|
◄ | ►
Back | Close

Full Screen / Esc

Printer-friendly Version

Interactive Discussion

Bergan, T., Gallardo, L., and Rodhe, H.: Mercury in the global troposphere: a three-dimensional model study, Atmos. Environ., 33, 1575–1585, 1999.

Chang, J. C. and Hanna, S. R.: Air quality model performance evaluation, Meteorol. Atmos. Phys., 87, 167–196, doi:10.1007/s00703-003-0070-7, 2004.

Clarkson, T. W.: The toxicity of mercury and its compounds, in: Mercury Pollution: Integration and Synthesis, edited by: Watras, C. J. and Huckabee, J. W., Boca Raton, FL, USA, 631–641, 1994.

Cziczo, D. J., Nowak, J. B., Hu, J. H., and Abbatt, J. P. D.: Infrared spectroscopy of model tropospheric aerosols as a function of relative humidity: observation of deliquescence and crystallization, J. Geophys. Res.-Atmos., 102, 18843–18850, 1997.

Dibble, T. S., Zelie, M. J., and Mao, H.: Thermodynamics of reactions of ClHg and BrHg radicals with atmospherically abundant free radicals, Atmos. Chem. Phys., 12, 10271–10279, doi:10.5194/acp-12-10271-2012, 2012.

Donohoue, D. L., Bauer, D., and Hynes, A. J.: Temperature and pressure dependent rate coefficients for the reaction of Hg with Cl and the reaction of Cl with Cl: a pulsed laser photolysis-pulsed laser induced fluorescence Study, J. Phys. Chem. A, 109, 7732–7741, 2005.

Finlayson-Pitts, B. J.: Halogens in the troposphere, Anal. Chem., 82, 770–776, doi:10.1021/ac901478p, 2010.

Fischer, E. V., Ziemba, L. D., Talbot, R. W., Dibb, J. E., Griffin, R. J., Husain, L., and Grant, A. N.: Aerosol major ion record at Mount Washington, J. Geophys. Res.-Atmos., 112, D02303, doi:10.1029/2006JD007253, 2007.

Ghosal, S., Brown, M. A., Bluhm, H., Krisch, M. J., Salmeron, M., Jungwirth, P., and Hemminger, J. C.: Ion partitioning at the liquid/vapor interface of a multicomponent alkali halide solution: a model for aqueous sea salt aerosols, J. Phys. Chem. A, 112, 12378–12384, 2008.

Glasow, R. V., Sander, R., Bott, A., and Crutzen, P. J.: Modeling halogen chemistry in the marine boundary layer 1. Cloud-free MBL, J. Geophys. Res.-Atmos., 107, 9-1–9-16, 2002.

Goodsite, M. E., Plane, J. M. C., and Skov, H.: A theoretical study of the oxidation of HgO to HgBr$_2$ in the troposphere, Environ. Sci. Technol., 38, 1772–1776, 2004.

Goodsite, M. E., Plane, J. M. C., and Skov, H.: Erratum: A theoretical study of the oxidation of HgO to HgBr$_2$ in the troposphere, (Environ. Sci. Technol. (2004) 38:6 (1772–1776) doi:10.1021/es034680s), Environ. Sci. Technol., 46, 5262, doi:10.1021/es301201c, 2012.

Guha, S. and Francisco, J. S.: An ab initio study of the pathways for the reaction between CH$_3$O$_2$ and BrO radicals, J. Chem. Phys., 118, 1779–1793, doi:10.1063/1.1531099, 2003.

Title Page

Abstract | Introduction

Conclusions | References

Tables | Figures

◄ | ►

◄ | ►

Back | Close

Full Screen / Esc

Printer-friendly Version

Interactive Discussion

Gustin, M. S., Amos, H. M., Huang, J., Miller, M. B., and Heidecorn, K.: Measuring and modeling mercury in the atmosphere: a critical review, Atmos. Chem. Phys., 15, 5697–5713, doi:10.5194/acp-15-5697-2015, 2015.

Hall, B.: The gas phase oxidation of elemental mercury by ozone, Water Air Soil Poll., 80, 301–315, 1995.

Hanna, S. R.: Air quality model evaluation and uncertainty, JAPCA J. Air Waste Ma., 38, 406–412, doi:10.1080/08940630.1988.10466390, 1988.

Hanna, S. R., Strimaitis, D. G., and Chang, J. C.: Hazard response modeling uncertainty (a quantitative method), vol. I: User's guide for software for evaluating hazardous gas dispersion models; vol. II: Evaluation of commonly-used hazardous gas dispersion models; vol. III: Components of uncertainty in hazardous gas dispersion models, Sigma Research Corporation, Westford, USA, 1991.

Hanna, S. R., Chang, J. C., and Strimaitis, D. G.: Hazardous gas model evaluation with field observations, Atmos. Environ. A-Gen., 27, 2265–2285, doi:10.1016/0960-1686(93)90397-H, 1993.

Hedgecock, I. M. and Pirrone, N.: Chasing quicksilver: modeling the atmospheric lifetime of Hg 0(g) in the marine boundary layer at various latitudes, Environ. Sci. Technol., 38, 69–76, 2004.

Hedgecock, I. M. and Pirrone, N.: Modelling chemical and physical processes of Hg compounds in the marine boundary layer, Dyn. Mercury Pollut. Reg. Glob. Scales Atmospheric Process. Hum. Expo. World, 2005.

Hedgecock, I. M., Pirrone, N., Sprovieri, F., and Pesenti, E.: Reactive gaseous mercury in the marine boundary layer: modelling and experimental evidence of its formation in the Mediterranean region, Atmos. Environ., 37, S41–S49, 2003.

Hess, M., Krieger, U. K., Marcolli, C., Huthwelker, T., Ammann, M., Lanford, W. A., and Peter, T.: Bromine enrichment in the near-surface region of Br-doped NaCl single crystals diagnosed by rutherford backscattering spectrometry, J. Phys. Chem. A, 111, 4312–4321, 2007.

Holmes, C. D., Jacob, D. J., and Yang, X.: Global lifetime of elemental mercury against oxidation by atomic bromine in the free troposphere, Geophys. Res. Lett., 33, L20808, doi:10.1029/2006GL027176, 2006.

Holmes, C. D., Jacob, D. J., Mason, R. P., and Jaffe, D. A.: Sources and deposition of reactive gaseous mercury in the marine atmosphere, Atmos. Environ., 43, 2278–2285, 2009.

Title Page

Abstract | Introduction

Conclusions | References

Tables | Figures

|◀ | ▶|

◀ | ▶

Back | Close

Full Screen / Esc

Printer-friendly Version

Interactive Discussion

Holmes, C. D., Jacob, D. J., Corbitt, E. S., Mao, J., Yang, X., Talbot, R., and Slemr, F.: Global atmospheric model for mercury including oxidation by bromine atoms, Atmos. Chem. Phys., 10, 12037–12057, doi:10.5194/acp-10-12037-2010, 2010.

Jaffe, D. A., Lyman, S., Amos, H. M., Gustin, M. S., Huang, J., Selin, N. E., Levin, L., ter Schure, A., Mason, R. P., Talbot, R., Rutter, A., Finley, B., Jaeglé, L., Shah, V., McClure, C., Ambrose, J., Gratz, L., Lindberg, S., Weiss-Penzias, P., Sheu, G.-R., Feddersen, D., Horvat, M., Dastoor, A., Hynes, A. J., Mao, H., Sonke, J. E., Slemr, F., Fisher, J. A., Ebinghaus, R., Zhang, Y., and Edwards, G.: Progress on understanding atmospheric mercury hampered by uncertain measurements, Environ. Sci. Technol., 48, 7204–7206, doi:10.1021/es5026432, 2014.

Kim, P.-R., Han, Y.-J., Holsen, T. M., and Yi, S.-M.: Atmospheric particulate mercury: concentrations and size distributions, Atmos. Environ., 61, 94–102, 2012.

Kim, S. Y., Talbot, R., Mao, H., Blake, D. R., Huey, G., and Weinheimer, A. J.: Chemical transformations of Hg° during Arctic mercury depletion events sampled from the NASA DC-8, Atmos. Chem. Phys. Discuss., 10, 10077–10112, doi:10.5194/acpd-10-10077-2010, 2010.

Kutsher, J., Haikin, N., Sharon, A., and Heifetz, E.: On the formation of an elevated nocturnal inversion layer in the presence of a low-level jet: a case study, Bound.-Lay. Meteorol., 144, 441–449, doi:10.1007/s10546-012-9720-y, 2012.

Laskin, A., Moffet, R. C., Gilles, M. K., Fast, J. D., Zaveri, R. A., Wang, B., Nigge, P., and Shuttanandan, J.: Tropospheric chemistry of internally mixed sea salt and organic particles: surprising reactivity of NaCl with weak organic acids, J. Geophys. Res.-Atmos., 117, D15302, doi:10.1029/2012JD017743, 2012.

Laurier, F. and Mason, R.: Mercury concentration and speciation in the coastal and open ocean boundary layer, J. Geophys. Res.-Atmos., 112, D06302, doi:10.1029/2006JD007320, 2007.

Laurier, F. J. G., Mason, R. P., Whalin, L., and Kato, S.: Reactive gaseous mercury formation in the North Pacific Ocean's marine boundary layer: a potential role of halogen chemistry, J. Geophys. Res.-Atmos., 108, ACH3-1–ACH3-12, doi:10.1029/2003JD003625, 2003.

Lewis, E. R. and Schwartz, S. E.: Comment on "Size distribution of sea-salt emissions as a function of relative humidity," Atmos. Environ., 40, 588–590, doi:10.1016/j.atmosenv.2005.08.043, 2006.

Lin, C.-J. and Pehkonen, S. O.: Aqueous phase reactions of mercury with free radicals and chlorine: implications for atmospheric mercury chemistry, Chemosphere, 38, 1253–1263, 1999.

Lin, C.-J., Pongprueksa, P., Lindberg, S. E., Pehkonen, S. O., Byun, D., and Jang, C.: Scientific uncertainties in atmospheric mercury models I: Model science evaluation, Atmos. Environ., 40, 2911–2928, 2006.

Lindberg, S. E., Brooks, S., Lin, C.-J., Scott, K. J., Landis, M. S., Stevens, R. K., Goodsite, M., and Richter, A.: Dynamic oxidation of gaseous mercury in the arctic troposphere at polar sunrise, Environ. Sci. Technol., 36, 1245–1256, 2002.

Madronich, S.: UV radiation in the natural and perturbed atmosphere, in: Environmental Effects of UV, CRC Press, Boca Raton, FL, USA, available at: http://opensky.library.ucar.edu/collections/OSGC-000-000-020-698 (last access: 16 April 2015), 1993.

Mao, H. and Talbot, R.: O_3 and CO in New England: temporal variations and relationships, J. Geophys. Res.-Atmos., 109, D21304, doi:10.1029/2004JD004913, 2004.

Mao, H., Talbot, R. W., Sigler, J. M., Sive, B. C., and Hegarty, J. D.: Seasonal and diurnal variations of Hg° over New England, Atmos. Chem. Phys., 8, 1403–1421, doi:10.5194/acp-8-1403-2008, 2008.

Mao, H., Talbot, R., Hegarty, J., and Koermer, J.: Speciated mercury at marine, coastal, and inland sites in New England – Part 2: Relationships with atmospheric physical parameters, Atmos. Chem. Phys., 12, 4181–4206, doi:10.5194/acp-12-4181-2012, 2012.

Mason, R. P., Kim, E.-H., Cornwell, J., and Heyes, D.: An examination of the factors influencing the flux of mercury, methylmercury and other constituents from estuarine sediment, Mar. Chem., 102, 96–110, 2006.

Miller, C. L., Mason, R. P., Gilmour, C. C., and Heyes, A.: Influence of dissolved organic matter on the complexation of mercury under sulfidic conditions, Environ. Toxicol. Chem., 26, 624–633, 2007.

Moldanová, J. and Ljungström, E.: Sea-salt aerosol chemistry in coastal areas: a model study, J. Geophys. Res.-Atmos., 106, 1271–1296, doi:10.1029/2000JD900462, 2001.

Obrist, D., Tas, E., Peleg, M., Matveev, V., Faïn, X., Asaf, D., and Luria, M.: Bromine-induced oxidation of mercury in the mid-latitude atmosphere, Nat. Geosci., 4, 22–26, 2011.

Pal, B. and Ariya, P. A.: Gas-phase HO-initiated reactions of elemental mercury: kinetics, product studies, and atmospheric implications, Environ. Sci. Technol., 38, 5555–5566, 2004a.

Pal, B. and Ariya, P. A.: Studies of ozone initiated reactions of gaseous mercury: kinetics, product studies, and atmospheric implications, Phys. Chem. Chem. Phys., 6, 572–579, 2004b.

Title Page

Abstract · Introduction

Conclusions · References

Tables · Figures

◄ · ►

◄ · ►

Back · Close

Full Screen / Esc

Printer-friendly Version

Interactive Discussion

Pillai, P. S. and Moorthy, K. K.: Aerosol mass-size distributions at a tropical coastal environment: response to mesoscale and synoptic processes, Atmos. Environ., 35, 4099–4112, doi:10.1016/S1352-2310(01)00211-4, 2001.

Raofie, F. and Ariya, P. A.: Product study of the gas-phase BrO-initiated oxidation of Hg^0: Evidence for stable Hg^{1+} compounds, Environ. Sci. Technol., 38, 4319–4326, 2004.

Rolfhus, K. R., Sakamoto, H. E., Cleckner, L. B., Stoor, R. W., Babiarz, C. L., Back, R. C., Manolopoulos, H., and Hurley, J. P.: Distribution and fluxes of total and methylmercury in Lake Superior, Environ. Sci. Technol., 37, 865–872, 2003.

Rutter, A. P. and Schauer, J. J.: The impact of aerosol composition on the particle to gas partitioning of reactive mercury, Environ. Sci. Technol., 41, 3934–3939, doi:10.1021/es062439i, 2007.

Rutter, A. P., Shakya, K. M., Lehr, R., Schauer, J. J., and Griffin, R. J.: Oxidation of gaseous elemental mercury in the presence of secondary organic aerosols, Atmos. Environ., 59, 86–92, 2012.

Saiz-Lopez, A. and von Glasow, R.: Reactive halogen chemistry in the troposphere, Chem. Soc. Rev., 41, 6448–6472, doi:10.1039/C2CS35208G, 2012.

Saiz-Lopez, A., Shillito, J. A., Coe, H., and Plane, J. M. C.: Measurements and modelling of I_2, IO, OIO, BrO and NO_3 in the mid-latitude marine boundary layer, Atmos. Chem. Phys., 6, 1513–1528, doi:10.5194/acp-6-1513-2006, 2006.

Sander, R., Keene, W. C., Pszenny, A. A. P., Arimoto, R., Ayers, G. P., Baboukas, E., Cainey, J. M., Crutzen, P. J., Duce, R. A., Hönninger, G., Huebert, B. J., Maenhaut, W., Mihalopoulos, N., Turekian, V. C., and Van Dingenen, R.: Inorganic bromine in the marine boundary layer: a critical review, Atmos. Chem. Phys., 3, 1301–1336, doi:10.5194/acp-3-1301-2003, 2003.

Sander, S. P., Abbatt, J., Barker, J. R., Burkholder, J. B., Friedl, R. R., Golden, D. M., Huie, R. E., Kolb, C. E., Kurylo, M. J., Moortgat, G. K., Orkin, V. L., and Wine, P. H.: Chemical Kinetics and Photochemical Data for Use in Atmospheric Studies, Evaluation No. 17, JPL Publication 10-6, Jet Propulsion Laboratory, Pasadena, available at: http://jpldataeval.jpl.nasa.gov, 2011.

Sandu, A. and Sander, R.: Technical note: Simulating chemical systems in Fortran90 and Matlab with the Kinetic PreProcessor KPP-2.1, Atmos. Chem. Phys., 6, 187–195, doi:10.5194/acp-6-187-2006, 2006.

Schroeder, W. H. and Munthe, J.: Atmospheric mercury – an overview, Atmos. Environ., 32, 809–822, 1998.

Title Page

Abstract	Introduction
Conclusions	References
Tables	Figures

◄ | ►

◄ | ►

Back | Close

Full Screen / Esc

Printer-friendly Version

Interactive Discussion

Schwartz, S. E.: Mass-transport considerations pertinent to aqueous phase reactions of gases in liquid-water clouds, in: Chemistry of Multiphase Atmospheric Systems, edited by: Jaeschke, D. W., Springer, Berlin, Heidelberg, 415–471, available at: http://link.springer.com/chapter/10.1007/978-3-642-70627-1_16 (last access: 17 April 2015), 1986.

5 Selin, N. E., Javob, D. J., Park, R. J., Yantosca, R. M., Strode, S., Jaeglé, L., and Jaffe, D.: Chemical cycling and deposition of atmospheric mercury: global constraints from observations, J. Geophys. Res.-Atmos., 112, D02308, doi:10.1029/2006JD007450, 2007.

Shon, Z.-H., Kim, K.-H., Kim, M.-Y., and Lee, M.: Modeling study of reactive gaseous mercury in the urban air, Atmos. Environ., 39, 749–761, 2005.

10 Sigler, J. M., Mao, H., and Talbot, R.: Gaseous elemental and reactive mercury in Southern New Hampshire, Atmos. Chem. Phys., 9, 1929–1942, doi:10.5194/acp-9-1929-2009, 2009.

Sillman, S., Marsik, F. J., Al-Wali, K. I., Keeler, G. J., and Landis, M. S.: Reactive mercury in the troposphere: model formation and results for Florida, the northeastern United States, and the Atlantic Ocean, J. Geophys. Res.-Atmos., 112, D23305, doi:10.1029/2006JD008227, 2007.

15 Simpson, W. R., von Glasow, R., Riedel, K., Anderson, P., Ariya, P., Bottenheim, J., Burrows, J., Carpenter, L. J., Frieß, U., Goodsite, M. E., Heard, D., Hutterli, M., Jacobi, H.-W., Kaleschke, L., Neff, B., Plane, J., Platt, U., Richter, A., Roscoe, H., Sander, R., Shepson, P., Sodeau, J., Steffen, A., Wagner, T., and Wolff, E.: Halogens and their role in polar boundary-layer ozone depletion, Atmos. Chem. Phys., 7, 4375–4418, doi:10.5194/acp-7-4375-2007, 20 2007.

Simpson, W. R., Brown, S. S., Saiz-Lopez, A., Thornton, J. A., and von Glasow, R.: Tropospheric halogen chemistry: sources, cycling, and impacts, Chem. Rev., 115, 4035–4062, doi:10.1021/cr5006638, 2015.

Snider, G., Raofie, F., and Ariya, P. A.: Effects of relative humidity and CO(g) on the O_3-initiated 25 oxidation reaction of HgO(g): kinetic and product studies, Phys. Chem. Chem. Phys., 10, 5616–5623, 2008.

Soerensen, A. L., Sunderland, E. M., Holmes, C. D., Jacob, D. J., Yantosca, R. M., Skov, H., Christensen, J. H., Strode, S. A., and Mason, R. P.: An improved global model for air–sea exchange of mercury: high concentrations over the North Atlantic, Environ. Sci. Technol., 44, 30 8574–8580, 2010.

Steffen, A., Douglas, T., Amyot, M., Ariya, P., Aspmo, K., Berg, T., Bottenheim, J., Brooks, S., Cobbett, F., Dastoor, A., Dommergue, A., Ebinghaus, R., Ferrari, C., Gardfeldt, K., Goodsite, M. E., Lean, D., Poulain, A. J., Scherz, C., Skov, H., Sommar, J., and Temme, C.: A

synthesis of atmospheric mercury depletion event chemistry in the atmosphere and snow, Atmos. Chem. Phys., 8, 1445–1482, doi:10.5194/acp-8-1445-2008, 2008.

Subir, M., Ariya, P. A., and Dastoor, A. P.: A review of uncertainties in atmospheric modeling of mercury chemistry I. Uncertainties in existing kinetic parameters – fundamental limitations and the importance of heterogeneous chemistry, Atmos. Environ., 45, 5664–5676, 2011.

Talbot, R., Mao, H., and Sive, B.: Diurnal characteristics of surface level O_3 and other important trace gases in New England, J. Geophys. Res., 1 10, D09307, doi:10.1029/2004JD005449, 2005.

Tang, I. N., Tridico, A. C., and Fung, K. H.: Thermodynamic and optical properties of sea salt aerosols, J. Geophys. Res.-Atmos., 102, 23269–23275, 1997.

Tokos, J. J. S., Hall, B., Calhoun, J. A., and Prestbo, E. M.: Homogeneous gas-phase reaction of HgO with H_2O_2, O_3, CH_3I, and $(CH_3)_2S$: implications for atmospheric Hg cycling, Atmos. Environ., 32, 823–827, 1998.

Toyota, K., McConnell, J. C., Staebler, R. M., and Dastoor, A. P.: Air–snowpack exchange of bromine, ozone and mercury in the springtime Arctic simulated by the 1-D model PHANTAS – Part 1: In-snow bromine activation and its impact on ozone, Atmos. Chem. Phys., 14, 4101–4133, doi:10.5194/acp-14-4101-2014, 2014.

Verwer, J. G., Spee, E. J., Blom, J. G., and Hundsdorfer, W.: Second-order Rosenbrock method applied to photochemical dispersion problems, SIAM J. Sci. Comput., 20, 1456–1480, 1999.

Wang, F., Saiz-Lopez, A., Mahajan, A. S., Gómez Martín, J. C., Armstrong, D., Lemes, M., Hay, T., and Prados-Roman, C.: Enhanced production of oxidised mercury over the tropical Pacific Ocean: a key missing oxidation pathway, Atmos. Chem. Phys., 14, 1323–1335, doi:10.5194/acp-14-1323-2014, 2014.

Xie, Z.-Q., Sander, R., Pöschl, U., and Slemr, F.: Simulation of atmospheric mercury depletion events (AMDEs) during polar springtime using the MECCA box model, Atmos. Chem. Phys., 8, 7165–7180, doi:10.5194/acp-8-7165-2008, 2008.

Zhang, L., Wright, L. P., and Blanchard, P.: A review of current knowledge concerning dry deposition of atmospheric mercury, Atmos. Environ., 43, 5853–5864, 2009.

Zhang, L., Blanchard, P., Gay, D. A., Prestbo, E. M., Risch, M. R., Johnson, D., Narayan, J., Zsolway, R., Holsen, T. M., Miller, E. K., Castro, M. S., Graydon, J. A., Louis, V. L. S., and Dalziel, J.: Estimation of speciated and total mercury dry deposition at monitoring locations in eastern and central North America, Atmos. Chem. Phys., 12, 4327–4340, 2012.

Title Page

Abstract | Introduction

Conclusions | References

Tables | Figures

|◄ | ►|

◄ | ►

Back | Close

Full Screen / Esc

Printer-friendly Version

Interactive Discussion

Table 1. Gas phase Hg reactions in the box model.

No.	Reactions	Kinetic ($cm^3\,molecule^{-1}\,s^{-1}$)	Reference
G1	$Hg + O_3 \rightarrow HgO + O_2$	$8.43 \times 10^{-17} e^{-1407/T}$	Snider et al. (2008)
G2	$Hg + OH + O_2 \rightarrow HgO + HO_2$	$3.55 \times 10^{-14} e^{294/T}$	Pal and Ariya (2004)
G3	$Hg + H_2O_2 \rightarrow Hg(OH)_2$	8.5×10^{-19}	Tokos et al. (1998)
G4	$Hg + Cl \rightarrow HgCl$	$6.4 \times 10^{-13} e^{(680 \times (1/T - 1/298))}$	Donohoue et al. (2005)
G5	$Hg + Cl_2 \rightarrow HgCl_2$	2.6×10^{-18}	Ariya et al. (2002)
G6	$Hg + Br \rightarrow HgBr$	$3.7 \times 10^{-13} (T/298)^{-2.76}$	Goodsite et al. (2004, 2012)
G7	$Hg + BrO \rightarrow HgBrO$	1.8×10^{-14}	Raofie and Ariya (2004)
G8	$Hg + I \rightarrow HgI$	$4.0 \times 10^{-13} (T/298)^{-2.38}$	Goodsite et al. (2004)
G9	$HgI \rightarrow Hg + I$	$3.0 \times 10^{9} e^{-3742/T}$	Goodsite et al. (2004)
G10	$HgBr \rightarrow Hg + Br$	$1.6 \times 10^{-9} e^{-7801/T} \times [M]$	Dibble et al. (2012)
G11	$HgBr + Br \rightarrow Hg + Br_2$	3.89×10^{-11}	Balabanov et al. (2005)
G12	$HgBr + Br \rightarrow HgBr + Br$	3.97×10^{-11}	Balabanov et al. (2005)
G13	$HgBr + Br \rightarrow HgBr_2$	2.98×10^{-11}	Balabanov et al. (2005)
G14	$ClO + HgCl \rightarrow ClHgOCl$	5.0×10^{-11}	Dibble et al. (2012)
G15	$ClO + HgBr \rightarrow BrHgOCl$	5.0×10^{-11}	Dibble et al. (2012)
G16	$BrO + HgCl \rightarrow BrHgOCl$	1.09×10^{-10}	Dibble et al. (2012)[*]
G17	$BrO + HgBr \rightarrow BrHgOBr$	1.09×10^{-10}	Dibble et al. (2012), Wang et al. (2014)
G18	$NO_2 + HgCl \rightarrow ClHgNO_2$	8.6×10^{-11}	Dibble et al. (2012)[*]
G19	$NO_2 + HgBr \rightarrow BrHgNO_2$	8.6×10^{-11}	Dibble et al. (2012), Wang et al. (2014)
G20	$HO_2 + HgCl \rightarrow ClHgOOH$	8.2×10^{-11}	Dibble et al. (2012)[*]
G21	$HO_2 + HgBr \rightarrow BrHgOOH$	8.2×10^{-11}	Dibble et al. (2012), Wang et al. (2014)
G22	$OH + HgCl \rightarrow ClHgOH$	6.33×10^{-11}	Dibble et al. (2012)[*]
G23	$OH + HgBr \rightarrow BrHgOH$	6.33×10^{-11}	Dibble et al. (2012), Wang et al. (2014)
G24	$IO + HgBr \rightarrow BrHgOI$	4.9×10^{-11}	Wang et al. (2014)

[*] The kinetic data of these HgCl reactions were not included in Dibble et al. (2012), they were assumed as the same kinetic as the HgBr reactions, which were calculated by Wang et al. (2014).

Table 2. Box model input and simulated variables.

Parameter	Appledore Island (AI)	Thompson Farm (TF)	Pack Monadnock (PM)
Observed[1]			
RH, relative humidity	76.9	69.9	69.0
Temperature, °C	19.1	21.3	18.5
[GEM], ppqv	133.9	138.4	149.6
[O_3], ppbv	37.4	32.7	45.0
[NO], pptv	154.5	232.4	85.3
[CO], ppbv	169.6	156.2	120.2
Simulated[2]			
[Br], ppqv	28.50	0.20	0.18
[OH], ppqv	100.7	75.8	73.5
Other[3]			
v_d, cm s^{-1}, dry deposition velocity	GEM – 0.0045 GOM – 0.5 PBM – 0.5	GEM – 0.07 GOM – 1.2 PBM – 0.15	GEM – 0.08 GOM – 2.0 PBM – 0.25
H, M atm^{-1}, Henry's constants	HgO – 3.2×10^9 Hg(OH)$_2$ – 1.2×10^7 Other GOM – 2.7×10^9	HgO – 3.2×10^9 Hg(OH)$_2$ – 1.2×10^7 Other GOM – 2.7×10^9	HgO – 3.2×10^9 Hg(OH)$_2$ – 1.2×10^7 Other GOM – 2.7×10^9
L, m$^3_{water}$ m$^{-3}_{air}$, liquid water content	3×10^{-11}	1.25×10^{-11}	1×10^{-11}
D_g, m^2 s^{-1}, diffusion coefficient	1×10^{-5}	1×10^{-5}	1×10^{-5}
Z, m, boundary layer height	500	200–1120[4]	100
r_{dry}, μm, dry aerosol radius	3.5	0.3	0.07

[1] Observed 24 h mean values for all studied cases at these sites.
[2] Simulated 24 h mean values for all studied days at these sites.
[3] Reference: Baumgardner et al. (2000), Kim et al. (2012), Mao and Talbot (2004), Moldanová and Ljungström (2001), Pillai and Moorthy (2001), Shon et al. (2005), Zhang et al. 2009, 2012
[4] TF boundary layer height changed at each hour, the averaged diurnal cycle was obtained from Research Data Archive at the National Center for Atmospheric Research, http://rda.ucar.edu/.

Table 3. Sensitivity cases with varying physical and chemical parameters. The superscript D represents daytime and N nighttime. Downward arrows stand for decreases and upward arrows increases. T stands for the temperature diurnal cycle in the base case, and T + 10 K or T − 10 K represents 10 K higher temperature or 10 K lower temperature throughout the day respectively.

| Case No. | photolysis | Gas-droplet partitioning | | Rate Coefficients (cm^3 molec^{-1} s^{-1}) | | | Temp. | Results | |
		Include	Liquid water content (m$^3_{water}$ m$^{-3}_{air}$)	GEM + O$_3$ (298 K)	GEM + OH (298 K)	GEM + Br (298 K)		GOM	PBM
Base Case									
0	Yes	Yes	3.0×10^{-11}	7.5×10^{-19} [a]	9.5×10^{-14} [b]	3.7×10^{-13} [c]	T	–	–
Photochemistry									
1	No	Yes	3.0×10^{-11}	7.5×10^{-19}	9.5×10^{-14}	3.7×10^{-13}	T	↓21–80 % [D]	↓28–92 % [D]
Gas-particle partitioning									
2	Yes	No	–	7.5×10^{-19}	9.5×10^{-14}	3.7×10^{-13}	T	↑~ 280 %	↓100 %
Liquid water content									
3	Yes	Yes	3.0×10^{-12}	7.5×10^{-19}	9.5×10^{-14}	3.7×10^{-13}	T	↑~ 200 %	↓80 %
4	Yes	Yes	3.0×10^{-10}	7.5×10^{-19}	9.5×10^{-14}	3.7×10^{-13}	T	↓87 %	↑80 %
Reactions									
5	Yes	Yes	3.0×10^{-11}	3.0×10^{-20} [d]	9.5×10^{-14}	3.7×10^{-13}	T	↓15 % [D] ↓80 % [N]	↓5 % [N]
6	Yes	Yes	3.0×10^{-11}	–	9.5×10^{-14}	3.7×10^{-13}	T	↓19 % [D] ↓92 % [N]	↓5 % [N]
7	Yes	Yes	3.0×10^{-11}	7.5×10^{-19}	–	3.7×10^{-13}	T	↓10 % [D]	Negligible
8	Yes	Yes	3.0×10^{-11}	7.5×10^{-19}	9.5×10^{-14}	–	T	↓30 % [D]	↓45 % [D]
Temperature									
9	Yes	Yes	3.0×10^{-11}	7.5×10^{-19}	9.5×10^{-14}	3.7×10^{-13}	T + 10 K	↓9 % [D] ↑13 % [N]	↓9 % [D] ↑54 % [N]
10	Yes	Yes	3.0×10^{-11}	7.5×10^{-19}	9.5×10^{-14}	3.7×10^{-13}	T − 10 K	↑9 % [D] ↓11 % [N]	↑8 % [D] ↓28 % [N]

[a] Snider et al. (2008).
[b] Pal and Ariya (2004).
[c] Goodsite et al. (2004, 2012).
[d] Hall (1995).

Table 4. Possible pathways of BrO + CH_3O_2 reaction.

No.	Reactions	Kinetics ($cm^3\,molecule^{-1}\,s^{-1}$)	Reference
B1	$BrO(g) + CH_3O_2(g) \rightarrow CH_3O(g) + BrOO(g)$ $BrOO(g) \rightarrow Br(g) + O_2(g)$	1.4×10^{-12} Fast	Aranda et al. (1997), Atkinson et al. (2008)
B2	$BrO(g) + CH_3O_2(g) \rightarrow CH_2O_2(g) + HOBr(g)$	4.3×10^{-12}	Aranda et al. (1997), Atkinson et al. (2008)
B3	$BrO(g) + CH_3O_2(g) \rightarrow CH_3OBr(g) + O_2(g)$	?	Aranda et al. (1997)
B4	$BrO(g) + CH_3O_2(g) \rightarrow CH_3OOOBr(g) \rightarrow$ $CH_2O(g) + HOOBr(g)$	?	Guha and Francisco (2003)
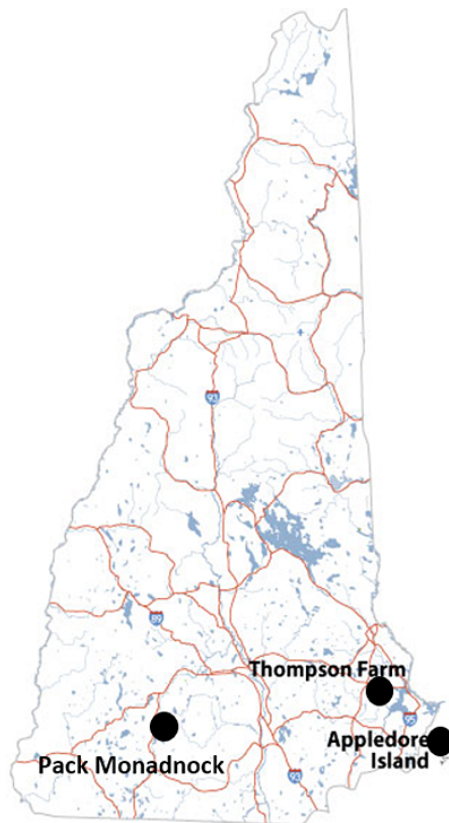
Figure 1. New Hampshire site map: Appledore Island (marine), Thompson Farm (coastal), and Pack Monadnock (inland elevated).
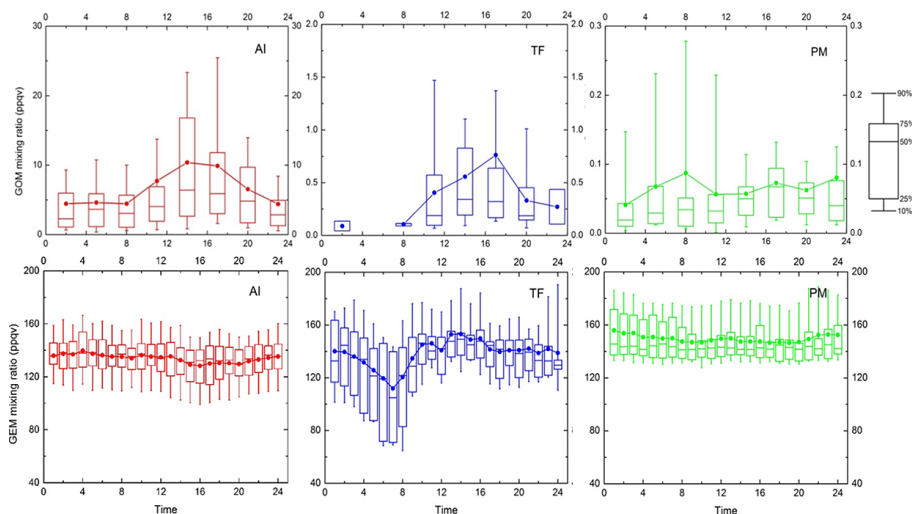
Figure 2. Average diurnal cycles and whisker diagrams of GOM and GEM observations over the selected 50 days at AI, 12 days at TF, and 21 days at PM from summers of 2007, 2008, and 2010.

Figure 3. Simulated average GOM diurnal cycles at AI **(a)**, TF **(b)**, and PM **(c)**. The bars suggest the range of GOM mixing ratios at each hour.

Title Page

Abstract | Introduction

Conclusions | References

Tables | Figures

|◄ | ►|

◄ | ►

Back | Close

Full Screen / Esc

Printer-friendly Version

Interactive Discussion
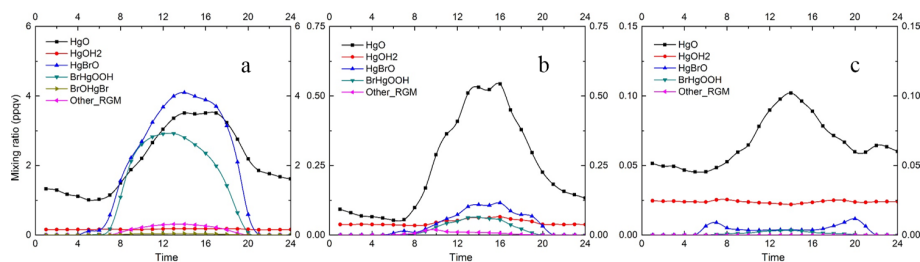
Figure 4. Simulated average diurnal cycles of GOM speciation at AI **(a)**, TF **(b)**, and PM **(c)**.

Title Page

Abstract · Introduction

Conclusions · References

Tables · Figures

|◄ · ►|

◄ · ►

Back · Close

Full Screen / Esc

Printer-friendly Version

Interactive Discussion
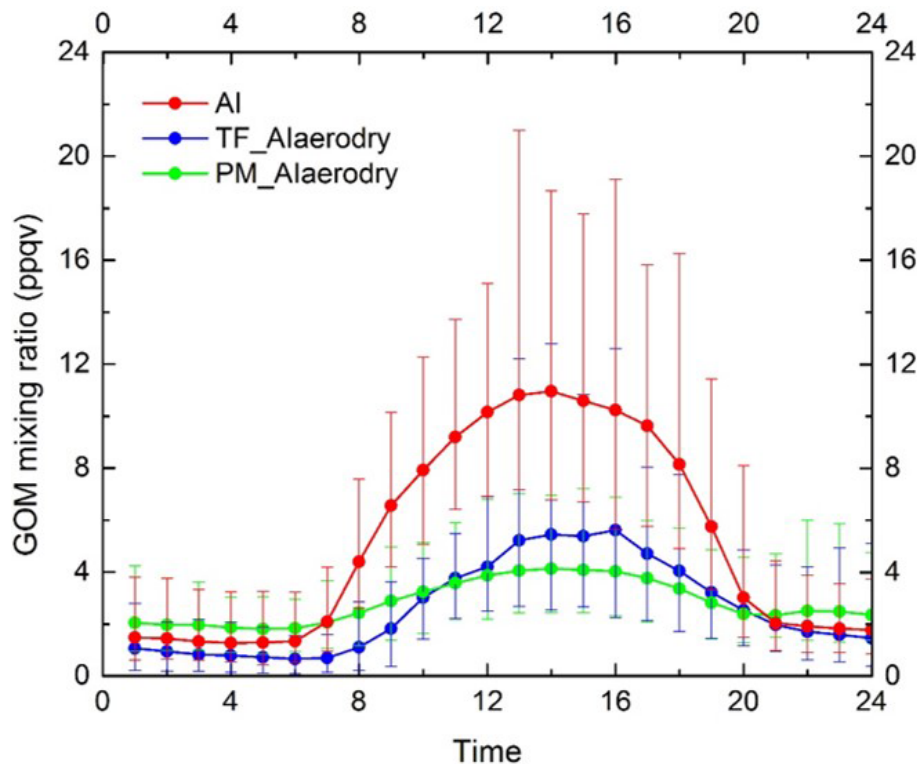
Figure 5. Simulated averaged diurnal cycles of GOM at AI (red), at TF (blue) using AI dry deposition and gas-aerosol partitioning parameters, and at PM (green) using AI dry deposition and gas-to-particle partitioning parameters.

Figure 6. Simulated diurnal cycles of Br (red) and BrO (blue) of the base case.
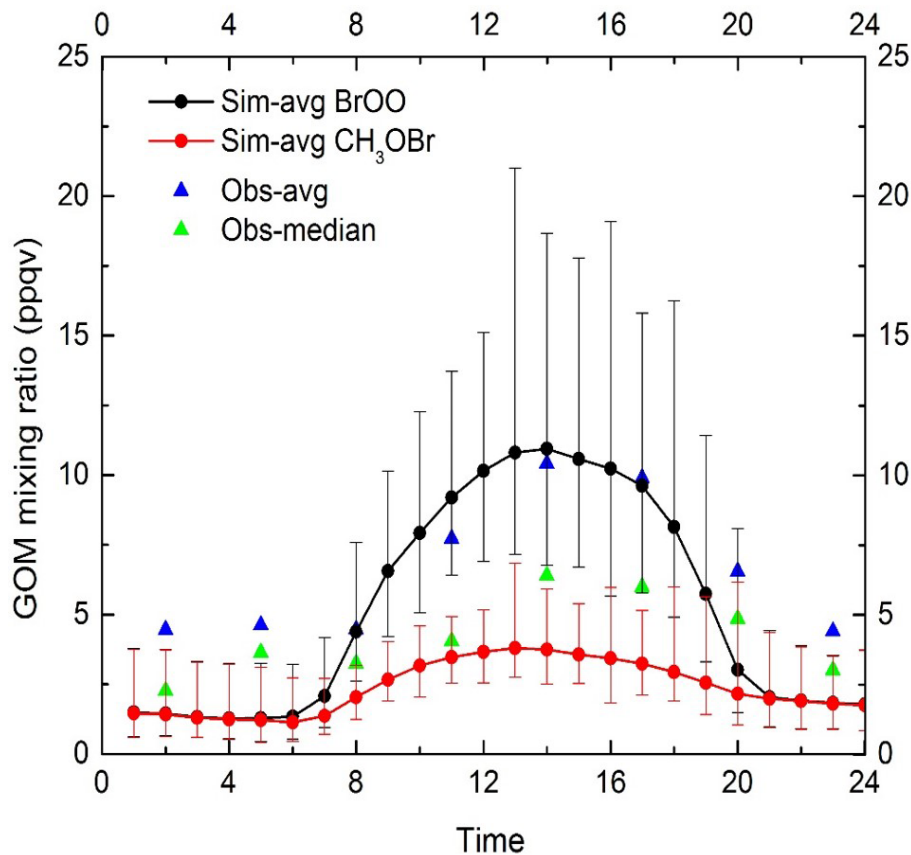
Figure 7. Simulated average diurnal cycles of GOM for the base case ("Sim-avg BrOO", black circle) and for the "CH_3OBr" case ("Sim-avg CH_3OBr", red, circle), observed average GOM diurnal cycle ("Obs-avg", blue, triangle scatter), and observed median GOM diurnal cycle ("Obs-median", green, triangle scatter) of the 50 cases at AI.

Figure 8. Comparison of simulated average ("Simulated", blue, circle) and observed average ("Observed", red, "Simulated", triangle) GOM diurnal cycles at AI **(a)**, TF **(b)**, and PM **(c)**. The error bars represent the standard deviation at each hour for all days.
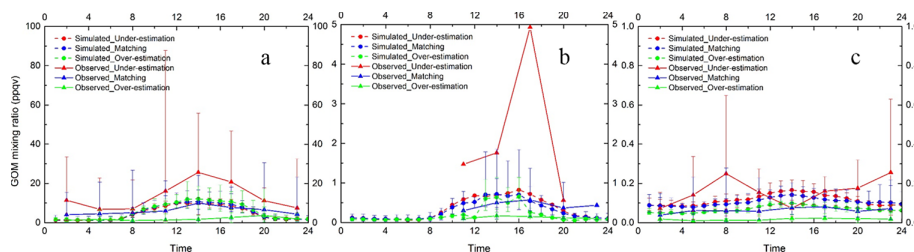
Figure 9. Observed (solid line) and simulated (dash line) average diurnal cycles of GOM for the matching (red), under-estimation (blue), and over-estimation cases (green) at AI **(a)**, TF **(b)**, and PM **(c)**. The bars represent the minimum and maximum mixing ratios at each hour for those specific days.
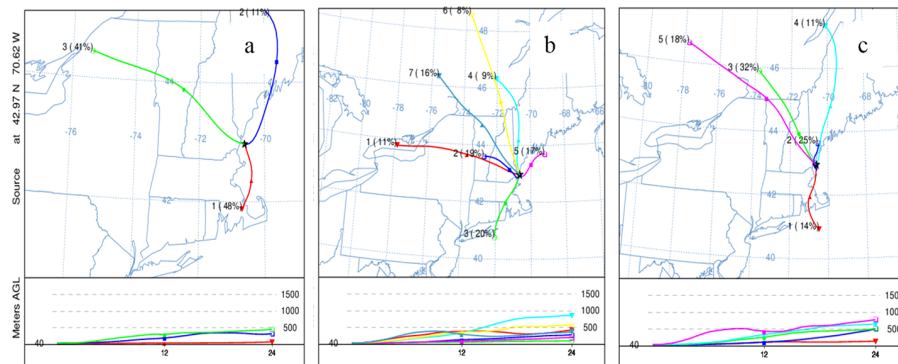
Figure 10. Clustered 24 h back trajectories of air masses in **(a)** over-estimation cases, **(b)** match cases, and **(c)** under-estimation cases at AI.